Journal of Solid State Chemistry 228 (2015) 160–166

Contents lists available at ScienceDirect

Journal of Solid State Chemistry

journal homepage: www.elsevier.com/locate/jssc

# Microwave sol–gel synthesis and upconversion photoluminescence properties of $CaGd_2(WO_4)_4$:$Er^{3+}$/$Yb^{3+}$ phosphors with incommensurately modulated structure

Chang Sung Lim [a], Aleksandr Aleksandrovsky [b,c], Maxim Molokeev [d,e], Aleksandr Oreshonkov [c,f], Victor Atuchin [g,h,i,*]

[a] Department of Advanced Materials Science & Engineering, Hanseo University, Seosan 356-706, Republic of Korea
[b] Laboratory of Coherent Optics, Kirensky Institute of Physics, SB RAS, Krasnoyarsk 660036, Russia
[c] Department of Photonics and Laser Technologies, Siberian Federal University, Krasnoyarsk 660079, Russia
[d] Laboratory of Crystal Physics, Kirensky Institute of Physics, SB RAS, Krasnoyarsk 660036, Russia
[e] Department of Physics, Far Eastern State Transport University, Khabarovsk 680021, Russia
[f] Laboratory of Molecular Spectroscopy, Kirensky Institute of Physics, SB RAS, Krasnoyarsk 660036, Russia
[g] Laboratory of Optical Materials and Structures, Institute of Semiconductor Physics, SB RAS, Novosibirsk 630090, Russia
[h] Functional Electronics Laboratory, Tomsk State University, Tomsk 634050, Russia
[i] Laboratory of Semiconductor and Dielectric Materials, Novosibirsk State University, Novosibirsk 630090, Russia

ARTICLE INFO

*Article history:*
Received 10 March 2015
Received in revised form
20 April 2015
Accepted 22 April 2015
Available online 1 May 2015

*Keywords:*
Double tungstate
Microwave sol–gel
Upconversion
XRD refinement
Raman

ABSTRACT

$CaGd_{2-x}(WO_4)_4$:$Er^{3+}$/$Yb^{3+}$ phosphors with the doping concentrations of $Er^{3+}$ and $Yb^{3+}$ ($x=Er^{3+}+Yb^{3+}$, $Er^{3+}=0.05$, 0.1, 0.2 and $Yb^{3+}=0.2$, 0.45) have been successfully synthesized by the microwave sol–gel method. The crystal structure of $CaGd_{2-x}(WO_4)_4$:$Er^{3+}$/$Yb^{3+}$ tungstates have been refined, and upconversion photoluminescence properties have been investigated. The synthesized particles, being formed after the heat-treatment at 900 °C for 16 h, showed a well crystallized morphology. Under the excitation at 980 nm, $CaGd_2(WO_4)_4$:$Er^{3+}$/$Yb^{3+}$ particles exhibited a strong 525-nm and a weak 550-nm emission bands in the green region and a very weak 655-nm emission band in the red region. The Raman spectrum of undoped $CaGd_2(WO_4)_4$ revealed about 12 narrow lines. The strongest band observed at 903 $cm^{-1}$ was assigned to the $\nu_1$ symmetric stretching vibration of $WO_4$ tetrahedrons. The spectra of the samples doped with Er and Yb obtained under the 514.5 nm excitation were dominated by $Er^{3+}$ luminescence preventing the recording of these samples Raman spectra. Concentration quenching of the erbium luminescence at $^2H_{11/2}\rightarrow{}^4I_{15/2}$ transition is weak in the range of erbium doping level $x_{Er}=0.05$–0.2, while, for transition $^4S_{3/2}\rightarrow{}^4I_{15/2}$, the signs of concentration quenching become pronounced at $x_{Er}=0.2$.



## 1. Introduction

The design and synthesis of new materials with desired and tunable properties continues to be a major goal of synthetic solid state chemists. One such class of materials is complex oxide photoluminescence crystals which exhibit different compositions and spectroscopic properties, high operation durability and emission efficiency, and a pronounced chemical stability in the air [1–11]. Recently, rare-earth-doped upconversion (UC) photoluminescence crystals have attracted great attention as functional materials for the frequency conversion from near infrared to visible spectral range [4,12–20]. These UC photoluminescence particles have potential applications in various fields including biomedical imaging, owing to their unique UC optical behavior that offers an improved light penetration depth, high chemical and photo stability, as well as the absence of auto-fluorescence during imaging, sharp emission bands and high resistance to photobleaching. These properties overcome many of the current limitations in traditional photoluminescence materials [18,21–24].

Recently, the compounds with a general composition of $MLn_2(TO_4)_4$ (M: Alkaline-earth or bivalent rare-earth metal ion, Ln: trivalent rare-earth ions, $T$=Mo, W) have been proposed as efficient phosphors [19,22,25–31]. The family can be further generalized as $M_xA_y(TO_4)_4$ (M: alkaline, alkaline-earth or bivalent rare-earth metal ion, A: trivalent lanthanide or actinide ion, $T$=Mo, W) under the charge balance condition $q(M)x+q(A)y=8$ [32–35]. As it can be reasonably supposed, the trivalent rare-earth ions in the

* Corresponding author at: Laboratory of Optical Materials and Structures, Institute of Semiconductor Physics, SB RAS, Novosibirsk 630090, Russia. Tel.: +7 383 3308889.
*E-mail address:* atuchin@isp.nsc.ru (V. Atuchin).

http://dx.doi.org/10.1016/j.jssc.2015.04.032
0022-4596/

disordered scheelite-type structure could be partially substituted by different $Ln^{3+}$ ions, and the ions are efficiently doped into the crystal lattice due to similar radii of $Ln^{3+}$ ions and that increases the restriction on the acceptable doping level. Among rare-earth ions, the $Er^{3+}$ ion is suitable for the infrared to visible light conversion through the UC process due to its appropriate electronic energy level configuration. The co-doped $Yb^{3+}$ ions can remarkably enhance the UC yield due to the efficient energy transfer from $Yb^{3+}$ to $Er^{3+}$. The $Er^{3+}$ ion activator is the luminescence center of the UC particles, while the $Yb^{3+}$ sensitizer enhances the UC luminescence efficiency [17–20,23,28,36].

The simple and double tungstate crystals are widely explored in laser and photonic technologies because of their specific structural, thermal and electronic characteristics, high chemical stability and excellent spectroscopic properties [37–45]. However, $MLn_2(WO_4)_4$ compounds are practically unstudied, and only tungstate solutions $CaGd_{2(1-x)}Eu_{2x}(WO_4)_4$ have recently been considered [30,31,46]. The powder samples were synthesized by solid state reaction at 1203 K [30,46]. For practical application of UC photoluminescence in products, such as lasers, three-dimensional displays, light-emitting devices and biological detectors, the features, such as the homogeneous UC particle size distribution and uniform morphology, need to be well defined. Usually, double tungstates are prepared by a multistep solid-state method that requires high temperatures, a lengthy heating process and subsequent grinding, this may occasionally result in a loss of the emission intensity. In comparison with that, the sol–gel process possesses some advantages including good particle homogeneity, low calcination temperature and a small particle size, and a narrow particle size distribution promising for good luminescent characteristics. However, the sol–gel process has a disadvantage of long gelation time. As compared to the usual methods, microwave synthesis has its advantages of a very short reaction time, small-size particles, narrow particle size distribution and high final polycrystalline products purity. Microwave heating is delivered to the material surface by radiant and/or convection heating which is transferred to the bulk of the material via conduction [47–51]. Thus, the microwave sol–gel process is an efficient method that provides high homogeneity powder products, and it is emerging as a viable alternative approach to the quick synthesis of high-quality luminescent materials. However, earlier, the synthesis of $MLn_2(WO_4)_4:Er^{3+}/Yb^{3+}$ phosphors by the microwave sol–gel process has not been reported on.

In the present study, the $CaGd_{2-x}(WO_4)_4:Er^{3+}/Yb^{3+}$ solid solutions with the doping concentrations of $Er^{3+}$ and $Yb^{3+}$ ($x=Er^{3+}+Yb^{3+}$, $Er^{3+}=0.05$, 0.1, 0.2 and $Yb^{3+}=0.2$, 0.45) were synthesized by the microwave sol–gel method, and the crystal structure refinement and UC photoluminescence properties evaluation were performed. The synthesized particles were characterized by X-ray diffraction (XRD), scanning electron microscopy (SEM), and energy-dispersive X-ray spectroscopy (EDS). The spectroscopic properties were examined comparatively using photoluminescence (PL) emission and Raman spectroscopy.

## 2. Experimental

Appropriate stoichiometric amounts of $Ca(NO_3)_2$ (99%, Sigma-Aldrich, USA), $Gd(NO_3)_3•6H_2O$ (99%, Sigma-Aldrich, USA), $(NH_4)_6W_{12}O_{39}•xH_2O$ (99%, Alfa Aesar, USA), $Er(NO_3)_3•5H_2O$ (99.9%, Sigma-Aldrich, USA), $Yb(NO_3)_3•5H_2O$ (99.9%, Sigma-Aldrich, USA), citric acid (99.5%, Daejung Chemicals, Korea), $NH_4OH$ (A.R.), ethylene glycol (A.R.) and distilled water were used as initial reagents to prepare the $CaGd_2(WO_4)_4$, $CaGd_{1.8}(WO_4)_4:Er_{0.2}$, $CaGd_{1.7}(WO_4)_4:Er_{0.1}Yb_{0.2}$, and $CaGd_{1.5}(WO_4)_4:Er_{0.05}Yb_{0.45}$ compounds with the doping concentrations of $Er^{3+}$ and $Yb^{3+}$ ($Er^{3+}=0.05$, 0.1, 0.2 and $Yb^{3+}=0.2$, 0.45).

To prepare $CaGd_2(WO_4)_4$, 0.4 mol% $Ca(NO_3)_2$ and 0.13 mol% $(NH_4)_6W_{12}O_{39}•xH_2O$ were dissolved in 20 mL of ethylene glycol and 80 mL of 5 M $NH_4OH$ under vigorous stirring and heating. Subsequently, 0.8 mol% $Gd(NO_3)_3•6H_2O$ and citric acid (with a molar ratio of citric acid to total metal ions content of 2:1) were dissolved in 100 mL of distilled water under vigorous stirring and heating. Then, the solutions were mixed together under vigorous stirring and heated at 80–100 °C. Finally, the highly transparent solutions were obtained and adjusted to pH=7–8 by the $NH_4OH$ or citric acid addition. In the second way, to prepare $CaGd_{1.8}(WO_4)_4:Er_{0.2}$, the mixture of 0.72 mol% $Gd(NO_3)_3•6H_2O$ and 0.08 mol% $Er(NO_3)_3•5H_2O$ was used to create the rare earth solution. In the third way, to prepare $CaGd_{1.7}(WO_4)_4:Er_{0.1}Yb_{0.2}$, the mixture of 0.68 mol% $Gd(NO_3)_3•6H_2O$ and 0.04 mol% $Er(NO_3)_3•5H_2O$, and 0.08 mol% $Yb(NO_3)_3•5H_2O$ was used to create the rare earth solution. In the fourth way, to prepare $CaGd_{1.5}(WO_4)_4:Er_{0.05}Yb_{0.45}$, the rare earth containing solution was generated using 0.6 mol% $Gd(NO_3)_3•6H_2O$ with 0.02 mol% $Er(NO_3)_3•5H_2O$ and 0.18 mol% $Yb(NO_3)_3•5H_2O$.

The transparent solutions were placed for 30 min into a microwave oven operating at the frequency of 2.45 GHz and the maximum output-power of 1250 W. The microwave reaction working cycle was being controlled very precisely between 40 s on and 20 s off for 15 min followed by a further treatment of 30 s on and 30 s off for 15 min. Ethylene glycol was evaporated slowly at its boiling point. Ethylene glycol is a polar solvent at its boiling point of 197 °C, and this solvent is a good medium for the microwave process. Respectively, if ethylene glycol is used as a solvent, the reactions proceed at the boiling point temperature. When microwave radiation is supplied to the ethylene-glycol-based solution, the components dissolved in the ethylene glycol can couple. The charged particles vibrate in the electric field interdependently when a large amount of microwave radiation is supplied to ethylene glycol. The samples were being treated with ultrasonic radiation for 10 min to produce a light yellow transparent sol. After this stage, the light yellow transparent sols were dried at 120 °C in a dry oven to obtain black dried gels. The black dried gels were being ground and heat-treated at 900 °C for 16 h in the air after several steps at 300 °C for 12 h, at 400–500 °C for 1 h and at 600–900 °C for 2 h with a 100 °C interval. Finally, the white particles were obtained for $CaGd_2(WO_4)_4$ and pink particles were obtained for the doped compositions.

The phase composition of the synthesized particles was evaluated using XRD (D/MAX 2200, Rigaku, Japan) with the scans over the range of $2\theta=5–110°$. The microstructure and surface morphology were observed using SEM/EDS (JSM-5600, JEOL, Japan). The PL spectra were recorded using a spectrophotometer (Perkin Elmer LS55, UK) at room temperature. Raman spectra measurements were performed using a LabRam Aramis (Horiba Jobin-Yvon, France) with the spectral resolution of 2 $cm^{-1}$. The 514.5-nm line of an Ar ion laser was used as an excitation source; the power on the samples was kept at 0.5 mW level to avoid the sample's decomposition.

## 3. Results and discussion

Previously, it was shown that the compounds within the $CaGd_{2(1-x)}Eu_{2x}(WO_4)_4$ series are (3+1)D incommensurately modulated with superspace group $I2/b(\alpha\beta0)00$ [30,44]. Therefore, first of all, the Le Bail decomposition was implemented using the JANA2006 software to prove incommensurability of the compounds under investigation [52]. The refinements were stable and gave low R-factors, as shown in Table 1. All the peaks in each pattern,

**Table 1**
Main parameters and processing of Le Bail fitting of the $CaGd_2(WO_4)_4$:*x*Er,*y*Yb samples using the (3+1)D modulation.

| Compound | $CaGd_2(WO_4)_4$ | $CaGd_{1.8}(WO_4)_4$:0.2Er | $CaGd_{1.7}(WO_4)_4$:0.1Er,0.2Yb | $CaGd_{1.5}(WO_4)_4$:0.05Er,0.45Yb |
|---|---|---|---|---|
| Sp.Gr. | $I2/b(\alpha\beta0)00$ | $I2/b(\alpha\beta0)00$ | $I2/b(\alpha\beta0)00$ | $I2/b(\alpha\beta0)00$ |
| q-vector | [5/9, 7/9, 0] | [0.5577(3), 0.7676(2), 0] | [0.5640(4), 0.7583(4), 0] | [0.5529(3), 0.7657(3), 0] |
| *a*, Å | 5.2202(4) | 5.2144(5) | 5.2165(7) | 5.2068(3) |
| *b*, Å | 5.2388(4) | 5.2378(5) | 5.2220(7) | 5.2294(3) |
| *c*, Å | 11.4085(7) | 11.400(1) | 11.374(1) | 11.3783(7) |
| γ, ° | 90.994(2) | 91.134(2) | 91.228(5) | 91.603(2) |
| *V*, Å$^3$ | 311.95(5) | 311.30(6) | 309.76(8) | 309.69(5) |
| $2\theta$-range, ° | 5–110 | 5–110 | 5–110 | 5–110 |
| $R_{wp}$, % | 12.55 | 14.09 | 18.43 | 12.79 |
| $R_p$, % | 8.82 | 10.01 | 13.32 | 8.98 |
| $R_{exp}$, % | 10.77 | 11.77 | 10.18 | 9.49 |
| $\chi^2$ | 1.17 | 1.20 | 1.81 | 1.35 |

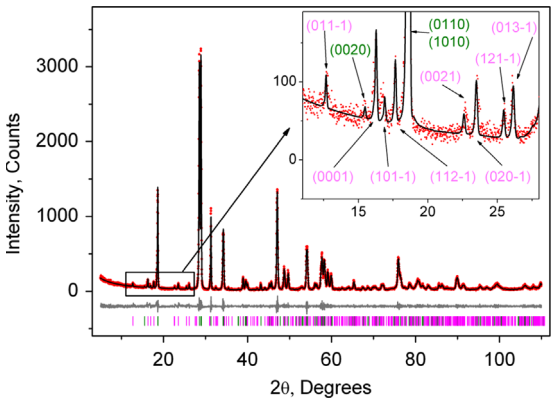


**Fig. 1.** A difference profile plot of $CaGd_2(WO_4)_4$. Red dots – experimental pattern ($Y_{obs}$), black line – calculated pattern ($Y_{calc}$), gray line – difference ($Y_{obs}$–$Y_{calc}$), green sticks – main Bragg peaks, purple – modulated peaks. The inset shows a zoomed part of the difference plot, the numbers in brackets show the reflection indices in the (3+1)D notation. (For interpretation of the references to color in this figure legend, the reader is referred to the web version of this article.)

excluding $CaGd_{1.7}(WO_4)_4$:0.1Er,0.2Yb, which contains a small impurity amount of $CaWO_4$ (15(1)%), were accounted by one phase, and this probes high phase purity of the samples. The refinement of undoped $CaGd_2(WO_4)_4$, as shown in Fig. 1, indicates the modulation q-vector coordinates close to 5/9 and 7/9. Therefore, these coordinates were fixed. The q-vector coordinates in doped compounds were refined independently and the results are shown in Table 1.

As far as it is not possible to calculate the vibrational spectra from the modulated crystal structure, the averaged crystal structure without modulation accounting was refined for each tungstate. Rietveld refinement was performed using TOPAS 4.2 [53]. In order to work with standard space groups, the *I2/b* non-standard setting was transformed to the *C2/c* standard setting using matrix (-1,-1,0; 0,0,-1; 1,0,0). The refinement was stable and gave low R-factors. The difference Rietveld plots are shown in Figs. 1S–4S. The resulted parameters are depicted in Table 2. The atom coordinates and main bond lengths are shown in Tables 1S and 2S, respectively. The determined crystal structure contains the $[WO_4]^{2-}$ tetrahedrons coordinated by four $(Ca/Gd/Er/Yb)O_8$ square antiprisms through common O ions, as shown in Fig. 2, where the structure of $CaGd_2(WO_4)_4$ is depicted. In the $CaGd_2(WO_4)_4$:$Er^{3+}$/$Yb^{3+}$ tungstates, the unit cell volume decreases proportionally to the integrated doping level *x* increase, as it is evident from Fig. 3. As it appears, the decrease seems to be due to known ionic radii relation $R(Gd^{3+}, CN=8)=1.053$, $R(Er^{3+}, CN=8)=1.004$ and $R(Yb^{3+}, CN=8)=0.985$ Å [54], and the substitution of big $Gd^{3+}$ ions by smaller $Er^{3+}$ and $Yb^{3+}$ ions is reasonably resulted in the unit cell shrinkage.

Thus, the microwave sol–gel route is suitable for the growth of the $CaGd_2(WO_4)_4$:$Er^{3+}$/$Yb^{3+}$ crystalline solid solutions similarly to the simple tungstates from the $CaWO_4$ family [14,16,48,55]. The post heat-treatment at 900 °C plays an important role in the formation of a well-defined microparticle morphology. It is evident, however, that the $Er^{3+}$/$Yb^{3+}$ doping level has a great effect for the unit cell volume of the tetragonal-phase solid solutions because of noticeably different rare-earth ion sizes. Also, it should be pointed that the XRD patterns recorded from several $MLn_2(MoO_4)_4$ molybdates were published and specific low intensity peaks could be found, especially over the low diffraction angles range [19,27,29]. The peaks, however, were not commented on or attributed to an admixture phase. Now, it can be reasonably supposed that these diffraction features appeared due to supestructure formation typical in $MLn_2(TO_4)_4$ crystals.

The SEM images of the synthesized $CaGd_2(WO_4)_4$:$Er^{3+}$/$Yb^{3+}$ particles are shown in Fig. 4. The samples crystallized with the formation of homogeneous partly agglomerated particles with the size of 1–3 μm. The well faceted tetragonal microcrystal forms were not found, and an irregular crystal form domination may be provided by a comparatively short synthesis time, when the equilibrium microcrystal forms were not obtained. The recorded EDS patterns and quantitative compositions of the $CaGd_{1.5}(WO_4)_4$:$Er_{0.05}Yb_{0.45}$ samples are shown in Fig. 5S. Only constituent elements are found in the samples and the quantitative compositions are in good relation with nominal compositions. This result confirms the persistence of the designed chemical composition during the microwave-modified sol–gel synthesis. It is emphasized that the microwave sol–gel process provides the energy uniformly to the bulk of the material, so that the fine particles with controlled morphology can be fabricated for a short time. The method is a cost-effective way to provide homogeneous double tungstate products with an easy scale-up potential, and it is a viable alternative for the rapid synthesis of UC particles.

The Raman spectrum recorded from $CaGd_2(WO_4)_4$ is shown in Fig. 5, and the spectrum decomposition can be found in Figs. 6S and 7S. About 12 narrow lines were revealed, and the total set of Raman lines observed in $CaGd_2(WO_4)_4$ is shown in Table 3. The Raman spectrum of $CaGd_2(WO_4)_4$ can be divided into two parts with a wide empty gap of 450–700 $cm^{-1}$ that is common in the tungstates with $WO_4$ tetrahedrons [56–61]. In the range of stretching vibrations of $WO_4$ tetrahedrons (700–950 $cm^{-1}$) five lines were observed. A vibrational representation for the monoclinic phase at the Brillouin zone center (with respect to occupancy) is:

$$\Gamma_{vibr} = 9A_g + 12B_g + 9A_u + 12B_u \quad (1)$$

The acoustic and optical modes are:

$$\Gamma_{acoustic} = A_u + 2B_u \quad (2)$$

**Table 2**
Main parameters of processing and Rietveld refinement the $CaGd_2(WO_4)_4$:*x*Er,*y*Yb samples by using average crystal structure.

| Compound | $CaGd_2(WO_4)_4$ | $CaGd_{1.8}(WO_4)_4$ :0.2Er | $CaGd_{1.7}(WO_4)_4$ :0.1Er,0.2Yb | $CaGd_{1.5}(WO_4)_4$ :0.05Er,0.45Yb |
|---|---|---|---|---|
| Space group | *C*2/*c* | *C*2/*c* | *C*2/*c* | *C*2/*c* |
| *a*, Å | 7.3392(3) | 7.3239(3) | 7.2924(5) | 7.3130(4) |
| *b*, Å | 11.4246(5) | 11.4120(5) | 11.3954(8) | 11.3851(6) |
| *c*, Å | 5.2242(2) | 5.2186(3) | 5.2099(4) | 5.2085(3) |
| *β*, ° | 134.368(2) | 134.279(2) | 134.91(4) | 134.325(2) |
| *V*, Å$^3$ | 313.20(3) | 312.28(3) | 310.91(4) | 310.23(3) |
| 2*θ*-range, ° | 5–110 | 5–110 | 5–110 | 5–110 |
| Number of reflections | 208 | 208 | 208 | 208 |
| Number of refined parameters | 36 | 36 | 36 | 36 |
| $R_{wp}$, % | 16.10 | 17.51 | 19.26 | 17.04 |
| $R_p$, % | 11.20 | 12.15 | 13.48 | 11.70 |
| $R_{exp}$, % | 10.76 | 11.75 | 10.16 | 9.48 |
| $\chi^2$ | 1.50 | 1.49 | 1.90 | 1.80 |
| $R_B$, % | 2.47 | 2.84 | 4.03 | 2.57 |

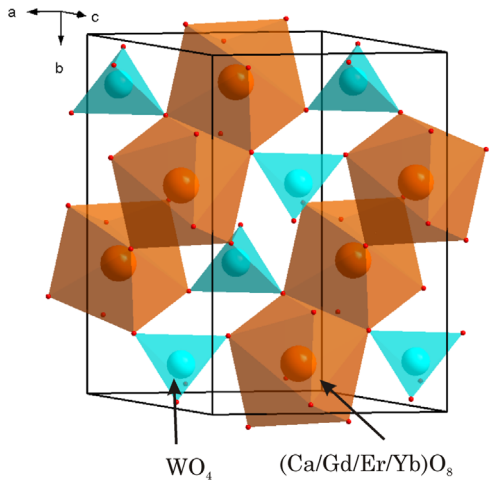


**Fig. 2.** The averaged crystal structure of $CaGd_2(WO_4)_4$. The unit cell is outlined. The lone atoms are omitted for clarity.

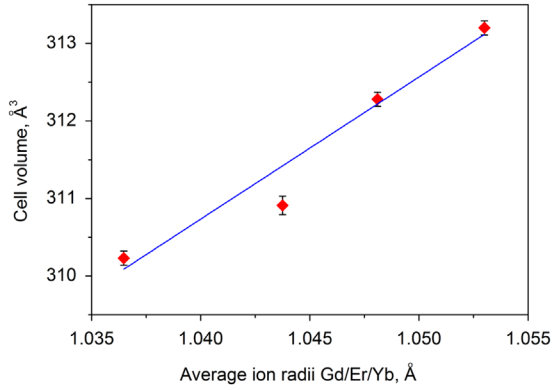


**Fig. 3.** The unit cell volume dependence of on x in the $CaGd_2(WO_4)_4$:$Er^{3+}$/$Yb^{3+}$ crystals.

$$\Gamma_{\text{optic}} = 9A_g + 12B_g + 8A_u + 10B_u \quad (3)$$

The infrared and Raman active modes are:

$$\Gamma_{\text{Raman}} = 9A_g + 12B_g \quad (4)$$

$$\Gamma_{\text{infrared}} = 8A_u + 10B_u \quad (5)$$

To calculate the $CaGd_2(WO_4)_4$ vibrational spectrum, the program package LADY was used [62]. The atomic vibration values were obtained using the modified random-element-isodisplacement model [63]. Previously, the optimized version of the model was tested for several compounds [64–66]. The model parameters obtained for $CaGd_2(WO_4)_4$ are shown in Table 4. The calculated parameters of the Raman active modes are shown in Table 3 in comparison with the experimental results.

The calculations show that only four Raman active modes should appear in the spectral range of $>700\ cm^{-1}$. The strong high-wavenumber band at $923\ cm^{-1}$ is assigned to the W–O (1) symmetric stretching vibration. The line at $942cm^{-1}$ corresponds to the W–O(1) anti-symmetric stretching vibration. The lines observed at 815 and $785\ cm^{-1}$ corresponds to the distorted $\nu_3$ $WO_4$ vibrations. The fifth active Raman mode in this spectral region, probably, appears due to the crystal structure modulation. Such assignment is supported by the XRD data. The $\nu_2$ and $\nu_4$ $WO_4$ bending modes are observed over the 250–450 $cm^{-1}$ range. Generally, the frequency of $\nu_2$ vibration should be lower than the frequency of $\nu_4$ vibration, the $\nu_2$ Raman band should be stronger than $\nu_4$, and $\nu_4$ can be hidden by $\nu_2$ in $[ReO_4]^{2-}$ spectra [67]. Our results are in agreement with the above-presented. The line at $205\ cm^{-1}$ is assigned to the Gd–O vibration.

The UC photoluminescence emission spectra of the as-prepared pure and doped $CaGd_{2-x}(WO_4)_4$ particles excited under 980 nm at room temperature are shown in Fig. 6. The $CaGd_{1.8}(WO_4)_4$:$Er_{0.2}$, $CaGd_{1.7}(WO_4)_4$:$Er_{0.1}Yb_{0.2}$ and $CaGd_{1.5}(WO_4)_4$:$Er_{0.05}Yb_{0.45}$ particles exhibit a strong emission band at 525 nm and a weak emission band at 550 nm in the green region, and the bands correspond to the $^2H_{11/2}\rightarrow{}^4I_{15/2}$ and $^4S_{3/2}\rightarrow{}^4I_{15/2}$ transitions, respectively. The very weak 655-nm emission band in the red region corresponds to the $^4F_{9/2}\rightarrow{}^4I_{15/2}$ transition. The UC intensity in the $CaGd_2(WO_4)_4$ has not been detected. The UC intensity of the $CaGd_{1.5}(WO_4)_4$:$Er_{0.05}Yb_{0.45}$ solid solution is much higher than those of the $CaGd_{1.8}(WO_4)_4$:$Er_{0.2}$, and $CaGd_{1.7}(WO_4)_4$:$Er_{0.1}Yb_{0.2}$ particles. Earlier, similar results were also observed from other $Er^{3+}$/$Yb^{3+}$ co-doped host matrices, which were assigned in the UC emission spectra with the green emission ($^2H_{11/2}\rightarrow{}^4I_{15/2}$ and $^4S_{3/2}\rightarrow{}^4I_{15/2}$ transitions) and the red emission ($^4F_{9/2}\rightarrow{}^4I_{15/2}$ transition) intensities [16,18,19,20,28,]. The $Er^{3+}$/$Yb^{3+}$ doping amounts greatly influenced the morphological features of the particles and their UC fluorescence intensity.

The $Yb^{3+}$ ion sensitizer in the $Er^{3+}$/$Yb^{3+}$ co-doped UC phosphors can be efficiently excited by the energy of an incident light source; this energy is transferred to the activator where radiation can be emitted. The $Er^{3+}$ ion activator is the luminescence center for these UC particles, and the sensitizer enhances the UC luminescence efficiency due to the energy matching of the gap between the $^2F_{7/2}$ and the $^2F_{5/2}$ of $Yb^{3+}$. The schematic energy level diagrams of $Er^{3+}$ ions (activator) and $Yb^{3+}$ ions (sensitizer) in the $CaGd_2(WO_4)_4$:$Er^{3+}$/$Yb^{3+}$ samples and the UC mechanisms

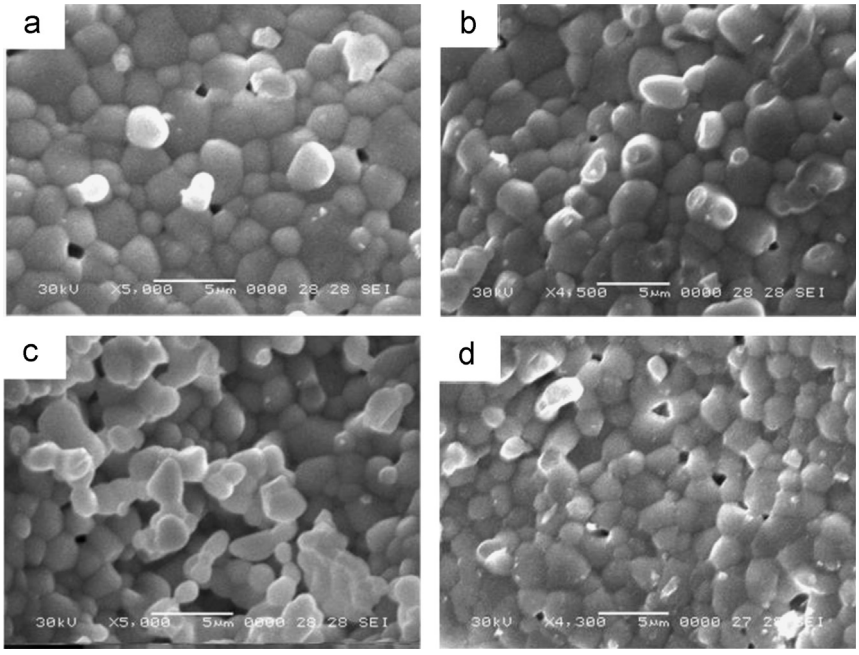


**Fig. 4.** Scanning electron microscopy images of the synthesized (a) $CaGd_2(WO_4)_4$, (b) $CaGd_{1.8}(WO_4)_4:Er_{0.2}$, (c) $CaGd_{1.7}(WO_4)_4:Er_{0.1}Yb_{0.2}$ and (d) $CaGd_{1.5}(WO_4)_4:Er_{0.05}Yb_{0.45}$ particles.

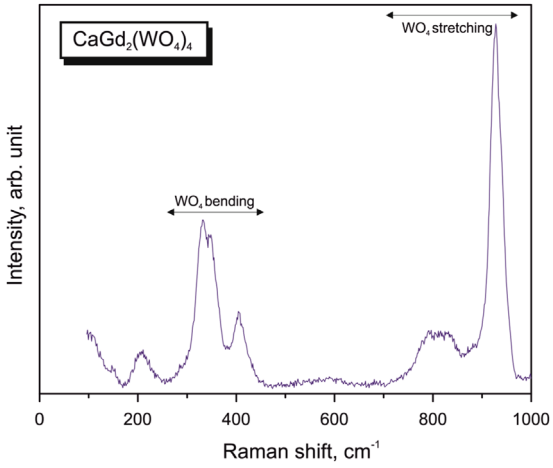


**Fig. 5.** The Raman spectrum of $CaGd_2(WO_4)_4$.

accounting for the green and red emissions at the 980 nm laser excitation are shown in Fig. 7. The UC emissions are generated through multiple processes of ground state absorption (GSA), energy transfer (ET), excited state absorption(ESA) and cross relaxation(CR). Under the excitation of 980 nm, the $Er^{3+}$ and $Yb^{3+}$ ions are initially excited from ground state to the excited state through the ground state absorptions (GSA) process ($Er^{3+}$: $^4I_{15/2}\rightarrow{}^4I_{11/2}$, $Yb^{3+}$: $^2F_{7/2}\rightarrow{}^2F_{5/2}$ ) and energy transfer (ET) process of $^4I_{15/2}$ ($Er^{3+}$)+$^2F_{5/2}$ ($Yb^{3+}$)→$^4I_{11/2}$ ($Er^{3+}$)+$^2F_{7/2}$ ($Yb^{3+}$) which are responsible for the population at the $^4I_{11/2}$ level in $Er^{3+}$ ion. For the green emissions, the energy transition from the $^4I_{11/2}$ level to the $^4F_{7/2}$ level of $Er^{3+}$ is involved into the three possible processes as follows [25,68–70]:

(1) ESA: $^4I_{11/2}$ ($Er^{3+}$)+a photon (980 nm)→$^4F_{7/2}$
(2) ET: $^2I_{11/2}$ ($Er^{3+}$)+$^2F_{5/2}$ ($Yb^{3+}$)→$^4F_{7/2}$ ($Er^{3+}$)+$^2F_{7/2}$ ($Yb^{3+}$)
(3) ET: $^4I_{11/2}$ ($Er^{3+}$)+$^4I_{11/2}$ ($Er^{3+}$)→$^4F_{7/2}$ ($Er^{3+}$)+$^4I_{15/2}$ ($Er^{3+}$)

These three possible processes can populate the $^4F_{7/2}$ level from the $^4I_{11/2}$ level in $Er^{3+}$, and then the $^4F_{7/2}$ level relaxes rapidly and non-radiatively to the next lower $^2H_{11/2}$ and $^4S_{3/2}$ levels in $Er^{3+}$ because of the short lifetime of the $^4F_{7/2}$ level. As a result, the radiative transitions of $^2H_{11/2}\rightarrow{}^4I_{15/2}$ and $^4S_{3/2}\rightarrow{}^4I_{15/2}$ processes can produce green emission at 525 and 550 nm. It is noted that the

**Table 3**
Calculated and experimental relative magnitude (*I*), wavenumber and full width at half maximum (FWHM) of the Raman lines.

| ω, ($cm^{-1}$ exp.) | *I* (exp.) | Γ (FWHM), ($cm^{-1}$, exp.) | Symm.type, (calc.) | ω ($cm^{-1}$, calc.) |
|---|---|---|---|---|
| 941 | 0.44 | 24 | $B_g$ | 942 |
| 925 | 1 | 21 | $A_g$ | 923 |
| 906 | 0.13 | 57 | | |
| 829 | 0.1 | 54 | $B_g$ | 815 |
| 785 | 0.11 | 48 | $A_g$ | 785 |
| 405 | 0.23 | 35 | $A_g$ | 401 |
| 360 | 0.2 | 22 | $B_g$ | 383 |
| 349 | 0.24 | 15 | $B_g$ | 338 |
| 330 | 0.56 | 27 | $A_g$ | 320 |
| 298 | 0.02 | 47 | $B_g$ | 297 |
| 217 | 0.01 | 74 | $B_g$ | 274 |
| 205 | 0.09 | 37 | $A_g$ | 254 |
| | | | $B_g$ | 202 |
| | | | $A_g$ | 188 |
| | | | $A_g$ | 186 |
| | | | $B_g$ | 179 |
| | | | $B_g$ | 110 |
| | | | $A_g$ | 102 |
| | | | $B_g$ | 91 |
| | | | $B_g$ | 60 |
| | | | $B_g$ | 52 |
| | | | $A_g$ | 49 |

**Table 4**
Parameters of the interatomic interaction potential.

| Interaction | λ (aJ/Å$^2$) | ρ (Å) |
|---|---|---|
| Ca–O | 311.06 | 0.3697 |
| Gd–O | 400.43 | 0.3024 |
| W–O(1) | 926.72 | 0.3346 |
| W–O(2) | 677.72 | 0.3662 |
| O–O | 325.17 | 0.3807 |

green upconversion luminescence can be induced by a two-photon process [25,68]. For the red emission, the $^4F_{9/2}$ level is generated by non-radiative relaxation from the $^4S_{3/2}$ to the $^4F_{9/2}$ level and cross relaxation (CR) $^4F_{7/2}+{}^4I_{11/2}\rightarrow{}^4F_{9/2}+{}^4F_{9/2}$ transition [69,70]. Finally, the $^4F_{9/2}$ level relaxes radiatively to the ground state at the $^4I_{15/2}$ level, and releases red emission at 655 nm [69,70]. The red emissions are so weak due to weak absorption cross relaxation. Moreover, as $Yb^{3+}$ concentration is increasing, the green emission dramtically increase compared to the red emission. The strong 525-nm and 550-nm emission bands in the green region, as shown in Fig. 6, are assigned to the $^2H_{11/2}\rightarrow{}^4I_{15/2}$ and $^4S_{3/2}\rightarrow{}^4I_{15/2}$ transitions of the $Er^{3+}$ ions, respectively, while the weak 655-nm emission band in the red region is assigned to the $^4F_{9/2}\rightarrow{}^4I_{15/2}$ transition. The much higher intensity of the $^2H_{11/2}\rightarrow{}^4I_{15/2}$ transition in comparison with the $^4S_{3/2}\rightarrow{}^4I_{15/2}$ transition in Fig. 6 may be induced by the concentration quenching effect due to the energy transfer between the nearest $Er^{3+}$ and $Yb^{3+}$ ions and the interactions between the doping ions in the host matrix [4,14,25]. This means that the green band induced by the $^4S_{3/2}\rightarrow{}^4I_{15/2}$transitions is assumed to be more easily quenched than the $^2H_{11/2}\rightarrow{}^4I_{15/2}$ transition by non-radiative relaxation in the case the case of the $CaGd_2(WO_4)_4$ host matrix.

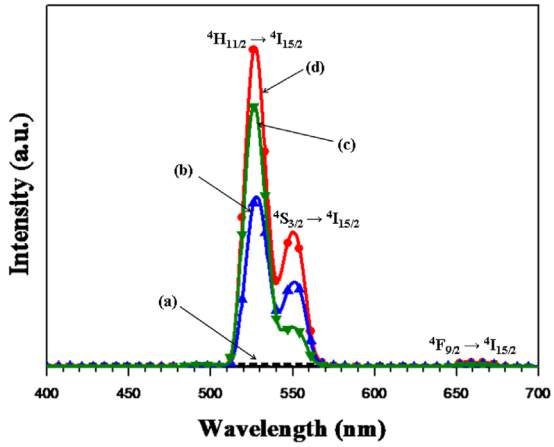


**Fig. 6.** The upconversion photoluminescence emission spectra of (a) $CaGd_2(WO_4)_4$, (b) $CaGd_{1.8}(WO_4)_4$:$Er_{0.2}$, (c) $CaGd_{1.7}(WO_4)_4$:$Er_{0.1}Yb_{0.2}$ and (d) $CaGd_{1.5}(WO_4)_4$:$Er_{0.05}Yb_{0.45}$ particles excited under 980 nm at room temperature.

The emission spectra of the Er-containing samples of $CaGd_{1.8}(WO_4)_4$:$Er_{0.2}$, $CaGd_{1.7}(WO_4)_4$:$Er_{0.1}Yb_{0.2}$ and $CaGd_{1.5}(WO_4)_4$:$Er_{0.05}Yb_{0.45}$ are shown in Fig. 8S. All the spectra were obtained under the excitation by a 514.5-nm line of an Ar ion laser at 0.5 mW on the samples. The spectrum of the undoped $CaGd_2(WO_4)_4$ sample is well interpreted in terms of Raman scattering, as described above. However, the shape of the spectra recorded from the samples doped with Er strongly differs from that of the undoped sample. At the same time, the shapes of the spectra of all Er-containing samples are very similar to each other and weakly vary with the erbium content, as well as with the presence of a large ytterbium content. The wavelength region, occupied by the spectra obtained in the erbium-doped samples excited at 514.5 nm, fairly coincides with the UC luminescence observed for them using the excitation at 980 nm, as well as with the well-known erbium luminescence in many other hosts (see, e.g. [10]). However, the relative luminescence intensity at $^2H_{11/2}\rightarrow{}^4I_{15/2}$ and $^4S_{3/2}\rightarrow{}^4I_{15/2}$ transitions under the excitation at 514.5 nm differs from the case of UC luminescence. This is understandable since, in case of UC, predominantly, the $^2F_{7/2}$ state is excited, while, under 514.5 nm irradiation, the excitation wavelength falls into a high-energy wing of the $^4I_{15/2}\rightarrow{}^2H_{11/2}$ transition. This leads to the difference in the populations of $^2H_{11/2}$ and $^4S_{3/2}$ in cases of UC and direct 514.5 nm excitation. The luminescence intensity at $^2H_{11/2}\rightarrow{}^4I_{15/2}$ transition is practically erbium concentration independent in the range $x=0.05$–$0.2$. Luminescence at the $^4S_{3/2}\rightarrow{}^4I_{15/2}$ transition is maximal in the range of $x=0.05$–$0.1$ and it shows a decrease for $x=0.02$, indicating the onset of concentration quenching. This is the difference between the $CaGd_2(WO_4)_4$ matrix and the previously studied $CaGd_2(MoO_4)_4$ crystal, where the influence of concentration quenching for both transitions is established approximately nearby the 10% erbium content, but it is slightly weaker for the $^4S_{3/2}\rightarrow{}^4I_{15/2}$ transition.

## 4. Conclusions

In the present study, the UC $CaGd_2(WO_4)_4$:$Er^{3+}$/$Yb^{3+}$ phosphors with appropriate doping concentrations of $Er^{3+}$ and $Yb^{3+}$ were successfully synthesized by the microwave sol-gel method. After the heat-treatment at 900 °C, the particles showed a well crystallized state. Under the excitation at 980 nm, $CaGd_{1.8}(WO_4)_4$:$Er_{0.2}$, $CaGd_{1.7}(WO_4)_4$:$Er_{0.1}Yb_{0.2}$ and $CaGd_{1.5}(WO_4)_4$:$Er_{0.05}Yb_{0.45}$

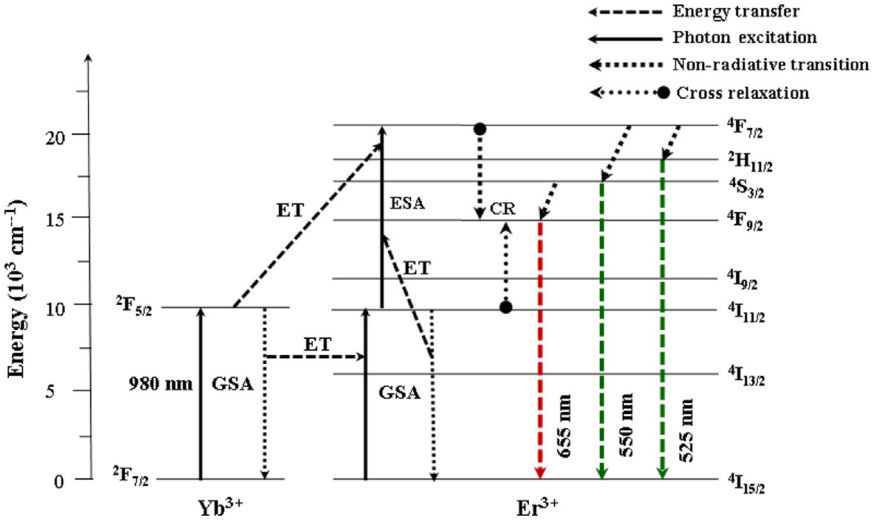


**Fig. 7.** The schematic energy level diagrams of $Er^{3+}$ ions (activator) and $Yb^{3+}$ ions (sensitizer) in the as-prepared $CaGd_2(WO_4)_4$:$Er^{3+}$/$Yb^{3+}$ system and the upconversion mechanisms accounting for the green and red emissions under 980-nm laser excitation. (For interpretation of the references to color in this figure legend, the reader is referred to the web version of this article.)

particles exhibited the 525-nm and 550-nm emission bands which were assigned to the $^2H_{11/2} \rightarrow {}^4I_{15/2}$, $^4S_{3/2} \rightarrow {}^4I_{15/2}$ and $^4F_{9/2} \rightarrow {}^4I_{15/2}$ transitions in $Er^{3+}$ ions. The UC intensity of $CaGd_{1.5}(WO_4)_4$:$Er_{0.05}Yb_{0.45}$ particles was much higher than those of the $CaGd_{1.8}(WO_4)_4$:$Er_{0.2}$ and $CaGd_{1.7}(WO_4)_4$:$Er_{0.1}Yb_{0.2}$ particles. Thus, the experiments confirm the efficient frequency upconversion process in the $CaGd_2(WO_4)_4$:$Er^{3+}$/$Yb^{3+}$ phosphor, the representative member of the $MLn_2(TO_4)_4$ family. The microwave synthesis combined with short-time annealing provides good cation ordering that was verified by the first structure determination of $CaGd_2(WO_4)_4$. This synthesis route could be widely used for other complex compounds from the $MLn_2(TO_4)_4$ family.

## Acknowledgments

This study was supported by the Basic Science Research Program through the National Research Foundation of Korea (NRF) funded by the Ministry of Science, ICT & Future Planning (2014-046024). VVA, ASA and ASO are partially supported by the Ministry of Education and Science of the Russian Federation.

## Appendix A. Supporting information

Supplementary data associated with this article can be found in the online version at http://dx.doi.org/10.1016/j.jssc.2015.04.032.

## References

[1] Nathan C. George, Kristin A. Denault, Ram Seshadri, Annu. Rev. Mater. Res. 43 (2013) 481–501.
[2] Mengmeng Shang, Chunxia Li, Jun Lin, Chem. Soc. Rev. 43 (2014) 1372–1386.
[3] Zhiguo Xia, Yuanyuan Zhang, Maxim S. Molokeev, Victor V. Atuchin, J. Phys. Chem. C, 117, 201320847–20854.
[4] Chang Sung Lim, Mater. Chem. Phys. 140 (1) (2013) 154–158.
[5] Takeshi Abe, Sun Woog Kim, Tadashi Ishigaki, Kazuyoshi Uematsu, Kenji Toda, Mineo Sato, Opt. Mater., 38, 201457–60.
[6] Zhiguo Xia, Yuanyuan Zhang, Maxim S. Molokeev, Victor V. Atuchin, Yi Luo, Sci. Rep. 3 (2013) 3310.
[7] Kai Li, Jian Fan, Xiaoyun Mi, Yang Zhang, Hongzhou Lian, Mengmeng Shang, Jun Lin, Inorg. Chem. 53 (2014) 12141–12150.
[8] Haikun Liu, Yuanyuan Zhang, Libing Liao, Qingfeng Guo, Lefu Mei, Ceram. Int., 40, 201413709–13713.
[9] Yiyao Peng, Zhipeng Lian, Lijing Zhang, Guangqiu Shen, Xiaoqing Wang, Qingfeng Yan, Mater. Express 4 (6) (2014) 533–538.
[10] A.V. Malakhovskii, T.V. Kutsak, A.L. Sukhachev, A.S. Aleksandrovsky A.S. Krylov, I.A. Gudim, M.S. Molokeev, Chem. Phys. 428 (2014) 137–143.
[11] Haipeng Ji, Zhaohui Huang, Zhiguo Xia, Maxim S. Molokeev, Victor V. Atuchin, Minghao Fang, Saifang Huang, Inorg. Chem. 53 (10) (2014) 5129–5135.
[12] J.F. Suyver, A. Aebischer, D. Biner, P. Gerner, J. Grimm, S. Heer, K.W. Krämer, C. Reinhard, H.U. Güdel, Opt. Mater. 27 (6) (2005) 1111–1130.
[13] M. Haase, H. Schäfer, Angew. Chem. Int. Ed. 50 (2011) 5808–5829.
[14] C.S. Lim, Mater. Res. Bull. 47 (2012) 4220–4225.
[15] Dengfeng Peng, Hua Zou, Chaonan Xu, Xusheng Wang, Xi Yao, J. Alloys Compd. 552 (2013) 463–468.
[16] C.S. Lim, V.V. Atuchin, Proc. SPIE 8771 (2013) 877110.
[17] M. Kochanowicz, D. Dorosz, J. Zmojda, J. Dorosz, P. Miluski, J. Lumin. 151 (2014) 155–160.
[18] V. Lojpur, G. Nikolic, M.D. Dramicanin, J. Appl. Phys. 115 (2014) 203106.
[19] C.S. Lim, Infr. Phys. Technol. 67 (2014) 371–376.
[20] A. Pandey, V.K. Rai, V. Kumar, V. Kumar, H.C. Swart, Sensors Actuat. B: Chem. 209 (2015) 352–358.
[21] M. Wang, G. Abbineni, A. Clevenger, C. Mao, S. Xu, Nanomed.: Nanotechnol. Biol. Med. 7 (2011) 710–729.
[22] Y.J. Chen, H.M. Zhu, Y.F. Lin, X.H. Gong, Z.D. Luo, Y.D. Huang, Opt. Mater. 35 (2013) 1422–1425.
[23] B.P. Singh, A.K. Parchur, R.S. Ningthoujam, P.V. Ramakrishna, S. Singh, P. Singh, S.B. Rai, R. Maalej, Phys. Chem. Chem. Phys. 16 (2014) 22665–22676.
[24] Jaehong Key, J.F. Leary, Int. J. Nanomed. 9 (2014) 711–726.
[25] H. Du, Y. Lan, Z. Xia, J. Sun, Mater. Res. Bull. 44 (2009) 1660–1662.
[26] M. Haque, D.K. Kim, Mater. Lett. 63 (2009) 793–796.
[27] C. Guo, H.K. Yang, J.H. Jeong, J. Lumin. 130 (2010) 1390–1393.
[28] J. Sun, Y. Lan, Z. Xia, H. Du, Opt. Mater. 33 (2011) 576–581.
[29] J. Liao, D. Zhou, B. Yang, R. Liu, Q. Zhang, Q. Zhou, J. Lumin., 134, 2013533–538.
[30] A.M. Abakumov, V.A. Morozov, A.A. Tsirlin, J. Verbeeck, J. Hadermann, Inorg. Chem. 53 (2014) 9407–9415.
[31] K.W. Meert, V.A. Morozov, A.M. Abakumov, J. Hadermann, D. Poelman P.F. Smet, Opt. Express 22 (S3) (2014) A961–A972.
[32] A. Tabuteau, M. Pages, J. Solid State Chem. 26 (1978) 153–158.
[33] N.D. Dahale, M. Keskar, K.D. Singh Mudher, J. Alloys Compd. 415 (2006) 244–250.
[34] N.D. Dahale, M. Keskar, N.K. Kulkarni, K.D. Singh Mudher, J. Alloys Compd. 440 (2007) 145–149.
[35] Gengbang Jin, L. Soderholm, J. Solid State Chem. 184 (2) (2011) 337–342.
[36] J. Sun, J. Xian, H. Du, J. Phys. Chem. Solids 72 (2011) 207–213.
[37] A.A. Kaminskii, H.J. Eichler, Ken-ichi Ueda, N.V. Klassen, B.S. Redkin, L.E. Li, J. Findeisen, D. Jaque, J. García-Sole, J. Fernández, R. Balda, Appl. Opt. 38 (21) (1999) 4533–4547.
[38] V.A. Isupov, Ferroelectrics 321 (2005) 63–90.
[39] V.V. Atuchin, V.G. Kesler, N.Y.u. Maklakova, L.D. Pokrovsky, Solid State Commun. 133 (2005) 347–351.
[40] V.V. Atuchin, V.G. Kesler, N.Y.U. Maklakova, L.D. Pokrovsky, D.V. Sheglov, Eur. Phys. J. B 51 (2) (2006) 293–300.
[41] Xiaoyu Liu, Shiliang Qu, Yang Tan, Feng Chen, Appl. Opt., 50, 2011930–934.
[42] A.M. Kaczmarek, R. Van Deun, Chem. Soc. Rev. 42 (2013) 8835–8848.
[43] B.I. Kidyarov, V.V. Atuchin, Ferroelectrics 444 (2013) 144–149.
[44] E.N. Galashov, V.V. Atuchin, A.S. Kozhukhov, L.D. Pokrovsky, V.N. Shlegel, J. Cryst. Growth 401 (2014) 156–159.
[45] Tzu-Chin Chien, Chii-Shyang Hwang, Masahiro Yoshimura, Yung-Tang Nien, Ceram. Int. 41 (2015) 155–161.
[46] V.A. Morozov, A. Bertha, K.W. Meert, S. Van Rompaey, D. Batuk, G.T. Martinez, S. Van Aert, P.F. Smet, M.V. Raskina, D. Poelman, A.M. Abakumov, J. Hadermann, Chem. Mater. 25 (2013) 4387–4395.
[47] S. Das, A.K. Mukhopadhyay, S. Datta, D. Basu, Bull. Mater. Sci. 32 (2009) 1–13.
[48] Chang Sung Lim, Mater. Chem. Phys. 131 (2012) 714–718.
[49] K.I. Rybakov, E.A. Olevsky, E.V. Krikun, J. Am. Ceram. Soc. 96 (4) (2013) 1003–1020.
[50] Victor Atuchin, Lei Zhu, Soo Hyun Lee, Dae Hyun Kim, Chang Sung Lim, Asian J. Chem. 26 (5) (2014) 1293–1296.
[51] H.J. Kitchen, S.R. Vallance, J.L. Kennedy, N. Tapia-Ruiz, L. Carassiti, A. Harrison, A.G. Whittaker, T.D. Drysdale, S.W. Kingman, D.H. Gregory, Chem. Rev. 114 (2014) 1170–1206.
[52] V. Petrícek, M. Dusek, L. Palatinus, Z. Kristallogr. 229 (5) (2014) 345–352.
[53] A.X.S. Bruker, TOPAS V4: General profile and structure analysis software for powder diffraction data. – User's Manual, Bruker AXS, Karlsruhe, Germany, 2008.
[54] R.D. Shannon, Acta Cryst. A 32 (1976) 751–767.
[55] V. Thangadurai, C. Knittlmayer, W. Weppner, Mater. Sci. Eng. B 106 (2004) 228–233.
[56] M. Maczka, A.G. Souza Filho, W. Paraguassu, P.T.C. Freire., J. Mendes Filho, J. Hanuza, Prog. Mater. Sci. 57 (2012) 1335–1381.
[57] S.P.S. Porto, J.F. Scott, Phys. Rev. 157 (3) (1967) 716–719.
[58] B.A. Kolesov, L.P. Kozeeva, J. Struct. Chem. 34 (4) (1993) 534–539.
[59] V.I. Tsaryuk, V.F. Zolin, B.F. Dzhurinskii, Zhurnal Neorganicheskoi Khimii 41 (1) (1996) 156–164.
[60] M. Maczka, Eur. J. Solid State Inorg. Chem. 33 (1996) 783–792.
[61] V.I. Tsaryuk, V.F. Zolin, Spectrochim. Acta A 57 (2001) 355–359.
[62] M.B. Smirnov, V.Y.u. Kazimirov, LADY: software for lattice dynamics simulations E 14-2001-159, JINR communications, 2001.
[63] I.F. Chang, S.S. Mitra, Phys. Rev. 172 (3) (1968) 924–933.
[64] A.S. Krylov, A.N. Vtyurin, A.S. Oreshonkov, V.N. Voronov, S.N. Krylova, J. Raman Spectr. 44 (5) (2013) 763–769.
[65] Zhiguo Xia, M.S. Molokeev, A.S. Oreshonkov, V.V. Atuchin, Ru-Shi Liu, Cheng Dong, Phys. Chem. Chem. Phys. 16 (2014) 5952–5957.
[66] A.A. Savina, V.V. Atuchin, S.F. Solodovnikov, Z.A. Solodovnikova, A.S. Krylov E.A. Maximovskiy, M.S. Molokeev, A.S. Oreshonkov, A.M. Pugachev E.G. Khaikina, J. Solid State Chem. 225 (2015) 53–58.
[67] K. Nakamoto, Infrared and Raman spectra of inorganic and coordination compounds, 6th edn, Wiley, New York etc., 2009.
[68] B. Li, B. Joshi, Y.K. Kshetri, R. Adhikari, R.N. Gracia, S.W. Lee, Opt. Mater. 39 (2015) 239–246.
[69] J.W. Lu, L. Cheng, J. Sun, H. Zhong, X. Li, Y. Tian, J. Wan, Y. Zheng, L. Huang, T. Yu, H. Yu, B. Chen, Phyica B 405 (2010) 3284–3288.
[70] J.H. Chung, J.I. Lee, S.L. Ryu, J.H. Ryu, Ceram. Int. 39 (2013) S369–S372.